POLITECNICO DI TORINO
Repository ISTITUZIONALE

Effective Inclusion of Sizable Amounts of Mo within TiO2 Nanoparticles Can Be Obtained by Reverse Micelle Sol-Gel Synthesis

(Article begins on next page)

18 October 2022

Effective Inclusion of Sizable Amounts of Mo within TiO₂ Nanoparticles Can Be Obtained by Reverse Micelle Sol−Gel Synthesis

Serena Esposito, Nicoletta Ditaranto, Gianfranco Dell'Agli, Roberto Nasi, Paola Rivolo, and Barbara Bonelli*

ACCESS | Metrics & More | Article Recommendations | SI Supporting Information

ABSTRACT: Six Mo/TiO₂ samples (with 0, 1.0, 2.5, 5.0, 7.5, and 10 wt % Mo nominal contents) were obtained by reverse micelle sol−gel synthesis, followed by calcination at 500 °C. The samples were characterized by means of powder X-ray Diffraction (PXRD), quantitative phase analysis as obtained by Rietveld refinement, field-emission scanning electron microscopy (FE-SEM) coupled with energy-dispersive X-ray analysis, N₂ adsorption/desorption at −196 °C, X-ray photoelectron spectroscopy, and diffuse reflectance (DR) UV−vis spectroscopy. As a whole, the adopted characterization techniques showed the inclusion of a sizeable Mo amount, without the segregation of any MoO$_x$ phase. Specifically, PXRD showed the occurrence of anatase and brookite with all the studied samples; notwithstanding the mild calcination temperature,

the formation of rutile occurred at Mo wt % ≥2.5 likely due to the presence of brookite favoring, in turn, anatase to rutile transition. DR UV−vis and XP spectroscopies allowed determining the samples' band gap energy (E_g) and valence band energy, respectively, from which the conduction band energy was calculated; and the observed E_g value increase at 10 wt % Mo was ascribed to the Moss−Burstein effect.
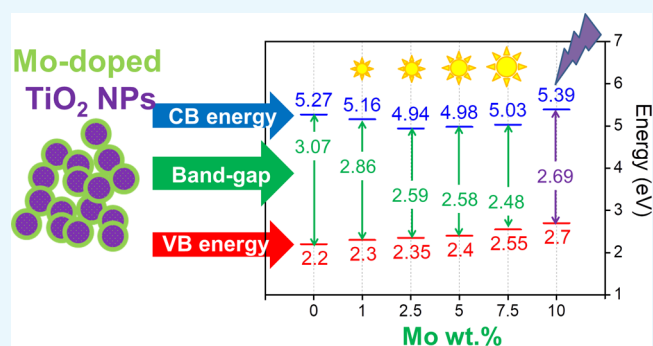
INTRODUCTION

TiO₂ is one of the most studied oxides due to its unique physicochemical properties, including the low toxicity and its availability in several morphologies, polymorphic composition, and nanoparticle (NP) size. Such reasons, along with its chemical stability and light absorption properties, allow its use in various fields, namely pigments, food additives, PPCPs (pharmaceuticals and personal care products), DSSC (dye-sensitized solar cells), and heterogeneous catalysis, particularly photocatalysis.[1−5]

Improving the ability to exploit solar light is particularly useful for photocatalytic applications because TiO₂ mostly absorbs in the UV range,[6−8] and doping with heteroatoms (either metals or nonmetals) is a widely adopted strategy to shift the absorption edge toward the vis range.[9−14] Doping may occur by different means leading to different results, and sometimes disappointing, i.e., when high dopant levels induce the formation of defects that, in turn, favor the electron/hole recombination, ultimately lowering the photocatalytic activity.[15−17]

Many literature methods that allow doping TiO₂, while simultaneously controlling the NP shape/size and type of polymorphic phase, imply the use of the sol−gel technique and the presence of a (soft or hard) template in order to induce (either intra- or interparticle) mesoporosity because the occurrence of mesopores is a desirable property, especially for catalytic and photocatalytic applications requiring a facile diffusion of reagents/products.[4,18−23]

Other doping methods provided fair results as well, including spray pyrolysis and magnetron sputtering,[24,25] laser ablation in solution,[26] hydrothermal synthesis,[27] etc. However, the availability of both diblock and triblock copolymers (acting as nonionic surfactants) and the EISA[28] (evaporation-induced self-assembly) technique (allowing the obtainment of uniform thin films) contributed to the widespread of template-assisted sol−gel techniques.[29] The use of a diblock copolymer in an organic solvent allows, indeed, the formation of reverse micelles having a hydrophobic shell and a hydrophilic core that acts as a nanoreactor, where NP nucleation and growth occur also in the presence of heteroatoms (here, Mo),

facilitating their effective inclusion in large(r) amounts and the size of NPs being determined by the micelle itself.[30,31] It has been previously reported that reverse micelles provide an acidic environment, leading to the occurrence of brookite-containing Mo-doped NP TiO_2:[13] the occurrence of brookite was found to play a role in the stabilization of electron/hole pairs during the photodegradation of rhodamine B under simulated solar light. Furthermore, the positive photocatalytic effect of brookite was also demonstrated with a set of (undoped) TiO_2 NPs toward the solar photodegradation of the emerging pollutant *N*-phenylurea.[18]

Concerning the doping mechanism(s), DFT (density functional theory) calculations have shown[32] that Mo 4d orbitals form impurity levels below the conduction band (CB) of TiO_2, whereas the Fermi level should not shift, finally improving the absorption of vis light in the resulting material. As mentioned before, the type of doping sites, *i.e.*, substitutional *versus* interstitial ones, is crucial[33,34] because the former has a prevailing role on the resulting TiO_2 electronic structure, red shift, and light absorption abilities. Both Mo_{VI}^{6+} and Mo_{VI}^{5+} species have an ionic radius (0.59 and 0.61 Å, respectively) allowing the isomorphic substitution of Ti_{VI}^{4+} ions (0.605 Å).[35] In order to balance the charge, the formation of Mo^{5+} species usually occurs (although a Mo_{VI}^{6+} precursor is used), otherwise, oxygen vacancies and/or Ti^{3+} species form.

In this work, a set of six samples with nominal Mo contents in the 0−10 wt % range was considered in order to provide an insight into the doping mechanism (interstitial *vs* substitutional); and the type of TiO_2 polymorphs and how, in turn, such polymorphs may affect the Mo inclusion or *vice versa*. Indeed, according to the literature, the rutile structure may accommodate heteroatoms/defects more easily than anatase, while the ATR (anatase to rutile) transition may be favored by brookite, whereas high valence dopant cations (charge >+4) disfavor ATR.[36]

The aim of this work is to effectively introduce, by reverse micelle sol−gel technique, sizable amounts of Mo in TiO_2 NPs in order to redshift their absorption onset and to lower the band gap energy. Furthermore, several complementary characterization techniques have been adopted in order to gain an insight into the type of Mo doping, the nature of Mo species and, consequently, the structural and surface properties of the obtained materials.

■ RESULTS AND DISCUSSION

Textural Properties of the Samples. Figure 1a shows the powder XRD patterns of the samples in the 20−90 2θ range. The TiO_2 sample showed the peaks of anatase (labeled A) at the 2θ values of 25.2 (101), 37.8 (004), 47.9 (200), 53.8 (105), 54.9 (211), 62.6 (204), 68.7 (116), 70.1 (220), 74.9 (125), and 82.5 (224); and the same sample also showed a broad and weak signal centred at *ca.* 30.7 2θ (labeled B), readily ascribed to the (121) diffraction peak of brookite, and the formation of which is favored at pH values as low as 2.0[18,37] and, here, was likely favored by the adopted synthesis procedure, implying extremely acidic conditions in the reverse micelle core. The Mo_1 sample showed very similar XRD patterns, albeit the (121) diffraction of brookite seemed less intense. At a higher Mo content (samples Mo_2.5, Mo_5, Mo_7.5, and Mo_10), two additional peaks (labeled R) were observed at 27.2 and 54.4 2θ values, respectively, assigned to the (110) and (211) diffraction peaks of rutile. Concerning the effect of Mo^{6+}/Mo^{5+} doping, especially on the reticular plane
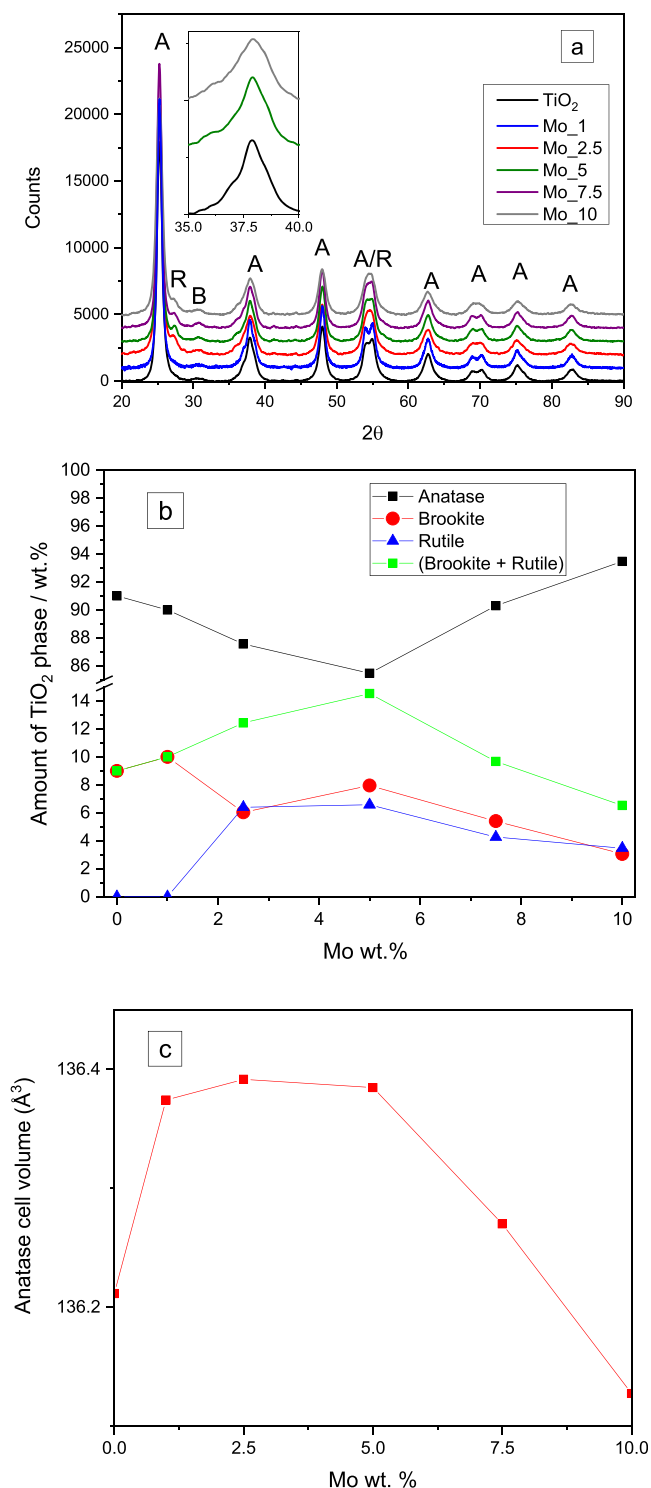

Figure 1. Powder XRD patterns of the studied samples (a); amounts of anatase, brookite, and rutile phases (wt %, as obtained by the Rietveld refinement) *vs* the samples' nominal composition (b); anatase cell volume (Å³, as obtained by the Rietveld refinement) *vs* the samples' nominal composition (c). Inset to section (a) reports a magnification of the 35−40 2θ range for a selected set of samples (namely, TiO_2, Mo_5, and Mo_10) for the sake of clarity.

of the various phases, a careful analysis of the 35−40 2θ range was carried out. The inset in Figure 1a shows a magnification of the 35−40 2θ range for the XRD patterns of the TiO_2, Mo_5, and Mo_10 samples only, in order to highlight possibly

Table 1. Textural Properties of the Studied Samples as Obtained by Powder XRD, FE-SEM, and EDX Analyses, N$_2$ Isotherms at −196 °C

sample	Mo wt %[a]	anatase wt %[b]	anatase crystal size (nm)[b]	brookite wt %[b]	rutile wt %[b]	average NP size (nm)[c]	BET SSA (m^2 g^{-1})	total pore volume (cm^3 g^{-1})
TiO$_2$		91.00	16.3	9.00		10.7	71	0.084
Mo_1	0.83	90.00	18.7	10		20.6	42	0.064
Mo_2.5	3.2	87.56	17.1	6.04	6.40	25	92	0.161
Mo_5	5.8	85.46	18.5	7.96	6.58	25.1	74	0.133
Mo_7.5	7.7	90.30	22.1	5.41	4.27	19.7	65	0.122
Mo_10	9.75	93.47	18.6	3.06	3.47	16.1	96	0.127

[a]As obtained by the EDX analysis [b]As obtained by the Rietveld refinement [c]As obtained by the FE-SEM analysis

relevant strain/stress phenomena, as reported by the literature in similar TiO$_2$-based materials.[38−40] After a careful analysis of the shape of the anatase (004) peak profiles, no relevant differences were, however, observed, likely due to the small difference in the cationic radii of octahedrally coordinated Ti^{4+}, Mo^{5+}, and Mo^{6+} ions (0.605, 0.61, and 0.59 Å, respectively).

Table 1 reports the corresponding quantative phase analysis (QPA) results, as obtained by the Rietveld refinement. Besides anatase, QPA showed the occurrence of brookite with all the samples, whereas the formation of rutile occurred at Mo wt % ≥2.5. Interestingly, no signals ascribable to any crystalline MoO$_x$ phase were detected, neither with the Mo_10 sample: on the one side, amorphous and/or extremely dispersed MoO$_x$ phases, if present, could escape the XRD detection, and on the other side, micro-Raman spectroscopy (Figure S1) shows the occurrence of the surface polymolibdate species (i.e., Mo$_7$O$_{24}$$^{6-}$ and Mo$_8$O$_{26}$$^{4-}$ species, where Mo was octahedrally coordinated) at a Mo content ≥5 wt %, without the MoO$_3$ segregation. Previous literature results[41] concerning samples at a comparable Mo content that were obtained by a microemulsion method showed the formation of both Mo surface species and MoO$_x$ phases, indicating that the reverse micelle sol−gel synthesis described here was more effective toward the inclusion of Mo in the TiO$_2$ matrix, likely because of the adopted surfactant.[42]

Figure 1b shows the trend of anatase and brookite (and rutile) wt % as a function of the sample nominal composition and the actual composition, as determined by the energy-dispersive X-ray (EDX) analysis, being indeed very close to the nominal one (Table 1), indicating the successful inclusion of Mo in the TiO$_2$ matrix by the adopted synthesis method. Interestingly, with the TiO$_2$, Mo_1, Mo_2.5, and Mo_5 samples, the anatase wt % decreases and, correspondingly, the brookite wt % increases, and the formation of rutile starts with the Mo_2.5 sample. At a higher Mo content (i.e., the Mo_7.5 and Mo_10 samples), the anatase wt % starts to increase again and, correspondingly, the overall amount of the other two phases decreases. The formation of rutile in the studied samples at the adopted calcination temperature (low for the ATR transition) is likely favored by the presence of brookite: the acidic environment of the reverse micelle core should indeed favor the formation of brookite which, in turn, favors the ATR transition according to the literature.[18,43] On the contrary, Mo^{6+} (and Mo^{5+}) species should inhibit the ATR transition: as reported by Hanaor et al.,[36] high charge cations (i.e., >+4) inhibit the rutile formation, whereas low charge cations (i.e., <+4) act as ATR transition promoters. Here, brookite likely promoted the ATR transition, being able to overcome the effect of Mo ions up to a 5 wt % Mo nominal content; and then, the effect of Mo ions became prominent

and, indeed, less rutile formed in the Mo_7.5 and Mo_10 samples, as it can be appreciated in Figure 1b.

Figure 1c reports, instead, the (Rietveld refinement determined) values of the anatase cell volume (Å^3), which first increase upon the inclusion of Mo, and then decrease (with the Mo_7.5 and Mo_10 samples). The increase of the cell volume with the increasing Mo content is reported by the literature,[44] as well as the cell volume decrease at a sufficiently higher Mo content.[45,46] Such a behavior can be explained by considering that, due to the similar ionic radii of Mo^{6+}/Mo^{5+} and Ti^{4+}, a substitutional solid solution forms, leading to an expansion of the unit cell. At a higher Mo concentration, the excess dopant ions cannot enter the TiO$_2$ lattice anymore, being therefore forced into interstitial sites, with the formation of defects, which, in turn, may lead to a unit cell volume decrease at a higher Mo concentration.[45] The Mo content, instead, does not affect the anatase crystallite size much, as shown by the corresponding values reported in Table 1. Unfortunately, the samples' low crystallinity did not allow the calculation of brookite and the rutile cell volume and crystallite size and thus, we could not monitor the occurrence of Mo doping in the other (less abundant) phase(s), although we are aware that the rutile structure is able to accommodate defects more efficiently than anatase.[47,48]

The morphological analysis, as carried out by FE-SEM, showed the occurrence of aggregated rounded particles (Figure S2). The corresponding particle size distributions and the NP average size values are reported in Figure 2a and in Table 1, respectively. As a whole, the TiO$_2$ sample shows smaller NPs than the Mo-doped ones; the NP size increases progressively with the Mo_1 and Mo_2.5 samples, and the latter having an average NP size very close to the Mo_5 sample. The Mo_5 sample, however, is characterized by a broader NP size distribution, as compared to the other samples. With both Mo_7.5 and Mo_10 samples, the NP average size decreases. The trend of NP average size as a function of the Mo nominal content is compared to that of the anatase cell volume (as obtained by the Rietveld refinement) in Figure 2b and, interestingly, the trends are similar, i.e., both parameters increase and, then, decrease with the Mo content, supporting the idea that Mo doping mainly occurs in the (most abundant) anatase phase.

Figure 3a shows the N$_2$ adsorption/desorption isotherms obtained at −196 °C on the studied samples, which showed type IV isotherms and type H2 hysteresis loop, typical of N$_2$ condensation within interparticle mesopores, and the corresponding BET SSA values are reported in Table 1. Figure 3b shows the corresponding PSD (pore size distribution) as obtained by applying the DFT method: as a whole, mesoporous samples were obtained, and their cumulative
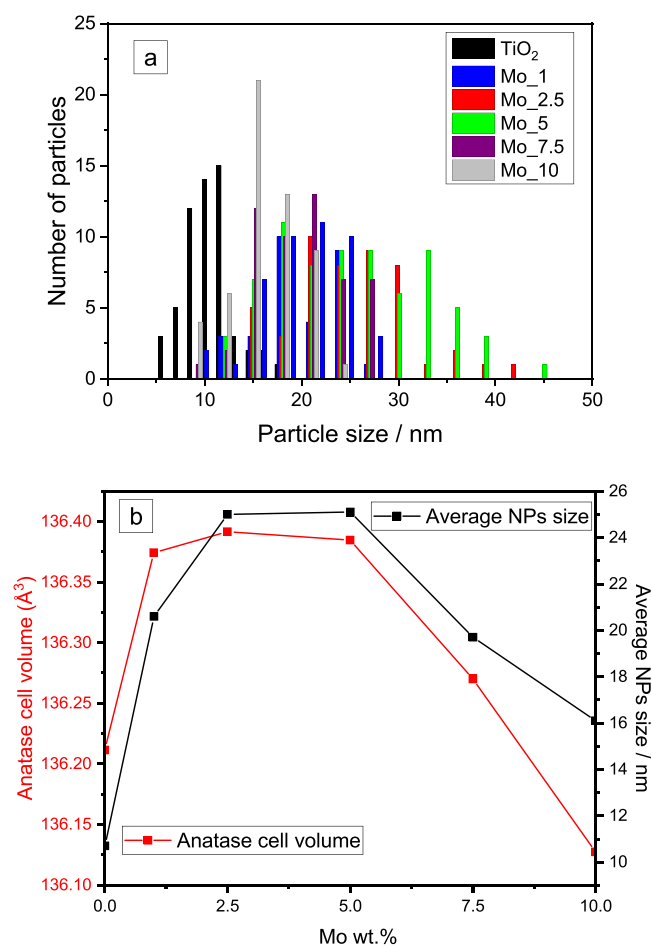
Figure 2. Particle size distribution as obtained by the FE-SEM analysis (a); average NP size (black curve, as obtained by the FE-SEM analysis) and anatase cell volume (red curve, as obtained by the Rietveld analysis,) *vs* the samples' nominal composition (b).

Figure 3. N$_2$ adsorption/desorption isotherms at −196 °C on the studied samples (a, full and empty symbols refer to adsorption and desorption run, respectively); PSD (pore size distribution) as obtained by applying the DFT method (b).

pore volume values are reported in Table 1. The Mo_2.5, Mo_5, and Mo_7.5 samples show broader PSD curves, in agreement with the fact that we are dealing with interparticle mesoporosity, and the same samples also showed broader NP size distributions (Figure 2a).

Bulk and Surface Composition. Table 2 reports, *inter alia*, the samples' bulk and surface composition, as determined by EDX and XPS analyses, respectively. As mentioned before, the EDX values were in fair agreement with the nominal ones, and the EDX maps (Figure S3) showed a uniform Mo distribution also with the Mo_10 sample. Although EDX is a semiquantitative technique, the adopted synthesis technique allows an effective inclusion of Mo, without the segregation of other phases, likely due to an optimized mixing of the Mo precursor and the Ti precursor within the reverse micelle core.

The XPS analysis was used to determine the samples' surface composition and allows us inferring possible differences between the surface and bulk composition. The XPS determined (surface) Mo/Ti at. % as a function of the EDX determined (bulk) Mo/Ti at. % (Figure 4) does not show a linear trend, but the tendency of Mo to sit at the NP surface and with the Mo_10 sample, the surface Mo/Ti at. % seems to reach a plateau. Such a "surface enrichment" is in agreement with micro-Raman spectroscopy (Figure S1 in the Supporting Information) showing the formation of surface polymolibdates at a higher Mo loading. Such a phenomenon could also affect
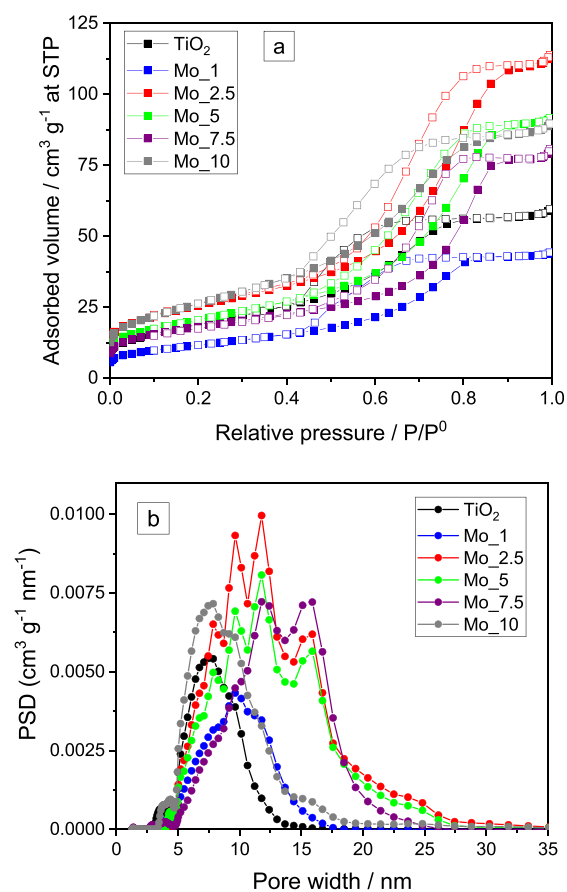
the surface acidity, which was studied by measuring the samples' electrophoretic mobility in water, with the determination of their ζ potential (Figure 5) and pH at isoelectric point (pH$_{IEP}$, Table 2). The inspection of the curves in Figure 5 allows some considerations to be drawn: first of all, the TiO$_2$ sample shows a lower pH$_{IEP}$ value as compared to the reported literature values for P25 (6.2−6.9)[49] and other types of TiO$_2$.[50−52] Such a phenomenon in the TiO$_2$ sample can be ascribed to the peculiar synthesis, which leads to the formation of an acidic surface, as already reported in the literature.[18,51] The (XPS determined) Mo enrichment of the samples' surface brings about a further increase in surface acidity, with progressive lowering of the pH$_{IEP}$ values, as the amount of Mo increases. Another point of interest is the measured value of ζ potential, which can be used to evaluate the stability of the suspension: usually, NP suspensions in water are stable with ζ potential values above +30 mV or below −30 mV.[53] In the examined pH range, stability is reached at basic pH with TiO$_2$ NPs and, to a minor extent, with Mo_2.5 NPs, indicating a tendency of the NPs to aggregate in water as the Mo content increases, indicating a modification of the NP surface. In Figure 5b, the measured pH$_{IEP}$ has been plotted as a function of the (XPS determined) surface Mo/Ti at. %: indeed, the pH$_{IEP}$ does not change sizably from sample Mo_1 to sample Mo_5, notwithstanding the progressive Mo surface enrichment. This likely means that the Mo is forming highly coordinated polymolibdate units, whereas at higher Mo

Table 2. Nominal Mo/Ti At. % Are Compared to the Total and Surface Mo/Ti At. % of the Studied Samples. XPS Determined Values of Surface Mo^{6+} and Mo^{5+} At. % and Valence Band Energies Are Also Reported (eV), along with DR UV−Vis Determined Band Gap Values (E_g, eV). pH$_{IEP}$ Values Have Been Determined from Electrophoretic Measurements

sample	nominal Mo/Ti at. %	total[a] Mo/Ti at. %	surface[b] Mo/Ti at. %	surface % of Mo^{6+} and Mo^{5+} species[b]		VB energy[b] (eV)	E_g (eV)[c]	pH$_{IEP}$
				Mo^{6+}	Mo^{5+}			
TiO$_2$	0	0	0			2.2	3.07	3.6
Mo_1	0.84	0.70	0.04	84	16	2.3	2.86	2.3
Mo_2.5	2.13	2.75	0.09	80	20	2.35	2.76	2.3
Mo_5	4.38	5.12	0.15	89	11	2.4	2.58	2.1
Mo_7.5	6.75	6.97	0.17	85	15	2.5	2.48	1.6
Mo_10	9.24	9.01	0.19	84	16	2.7	2.69	1.4

[a]As determined by the EDX analysis [b]As determined by the XPS analysis [c]As determined by applying the Tauc's plot method to the Kubelka−Munk DR spectra.
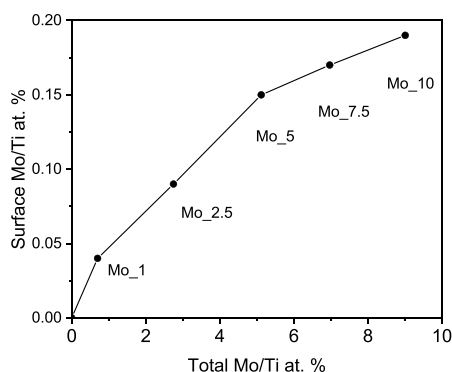

Figure 4. XPS determined surface Mo/Ti at. % vs EDX determined bulk Mo/Ti at. %.

contents, the pH decreases, indicating the formation of more acidic species, likely Mo−OH groups at the end of polymolibdate chains.

The oxidation state of the surface Mo species was also studied by XPS by applying a curve-fitting procedure to the Mo3d doublet of all the studied samples. Figure 6a shows the comparison of the Mo3d spectral regions, whereas Figure 6b shows a typical curve-fitting procedure for the Mo_2.5 sample. In all the studied cases, two doublets were used to properly interpret the spectral lines: the obtained binding energy (BE) values were compatible with the presence of both Mo^{6+} and Mo^{5+} surface species (BE Mo3d$_{5/2}$ = 231.3 $\pm$ 0.3 eV and BE Mo3d$_{5/2}$ = 232.5 $\pm$ 0.2 eV, respectively).[28]

After the curve-fitting procedure, the relative abundance of Mo^{6+}/Mo^{5+} species was obtained, and the corresponding values are reported in Table 2. The occurrence of surface Mo^{5+} species is not surprising because when isomorphic substitution occurs, the positive extra charges induced by the Mo^{6+} species have to be balanced by different means, namely the formation of oxygen vacancies, formation of (reduced) Mo^{5+} species, and reduction of Ti^{4+} to Ti^{3+} species. If those phenomena occur at the surface, they can be studied by XPS. Concerning the formation of reduced Ti^{3+} species, Figure 6c reports the position of the Ti2p$_{3/2}$ peak component as the surface Mo content (Mo/Ti at. %) increases: the Ti^{4+} peak position is seen to shift with progressive doping, but the observed Ti2p spin−orbit splitting is constant, indicating the unlikely formation of Ti^{3+} species at the surface.[54] To evaluate the occurrence of oxygen vacancies, the O1s spectral region was investigated and subjected to a curve-fitting procedure (Figure 6d shows, as an example, the results obtained with the Mo_7.5 sample). With
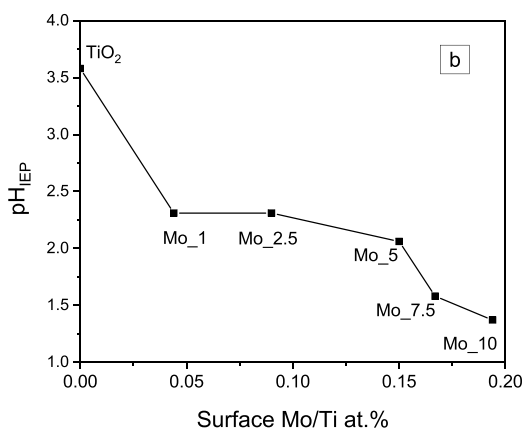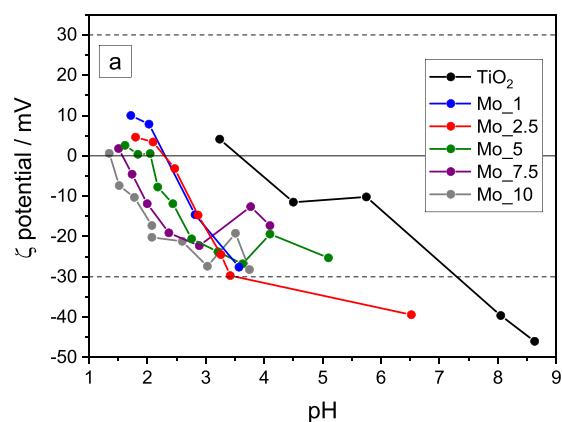

Figure 5. ζ potential curves for the studied samples (a); pH$_{IEP}$ values vs XPS determined surface Mo/Ti at. % (b).

all the samples, two peak components were found at BE = 529.8 $\pm$ 0.2 eV and BE = 530.8 $\pm$ 0.2 eV, ascribable to the lattice oxide species (M−O) and to oxygen species in the oxygen-deficient region, respectively.[55,56] The relative abundance of the oxygen vacancy component amounts to 15 $\pm$ 2% and is almost constant with the Mo content, with the exception of the Mo_5 sample in which the peak is less intense, and the amount of oxygen vacancies is equal to 9 $\pm$ 1%. The same sample also showed a lower amount of surface Mo^{5+} species; because XPS allows the study of surface species, (further) oxygen vacancies and/or Mo^{5+} species could be located in the bulk of Mo_5 NPs, finally escaping XPS detection.

Furthermore, by XPS it was also possible to measure the position of the valence band (VB) energy (the corresponding
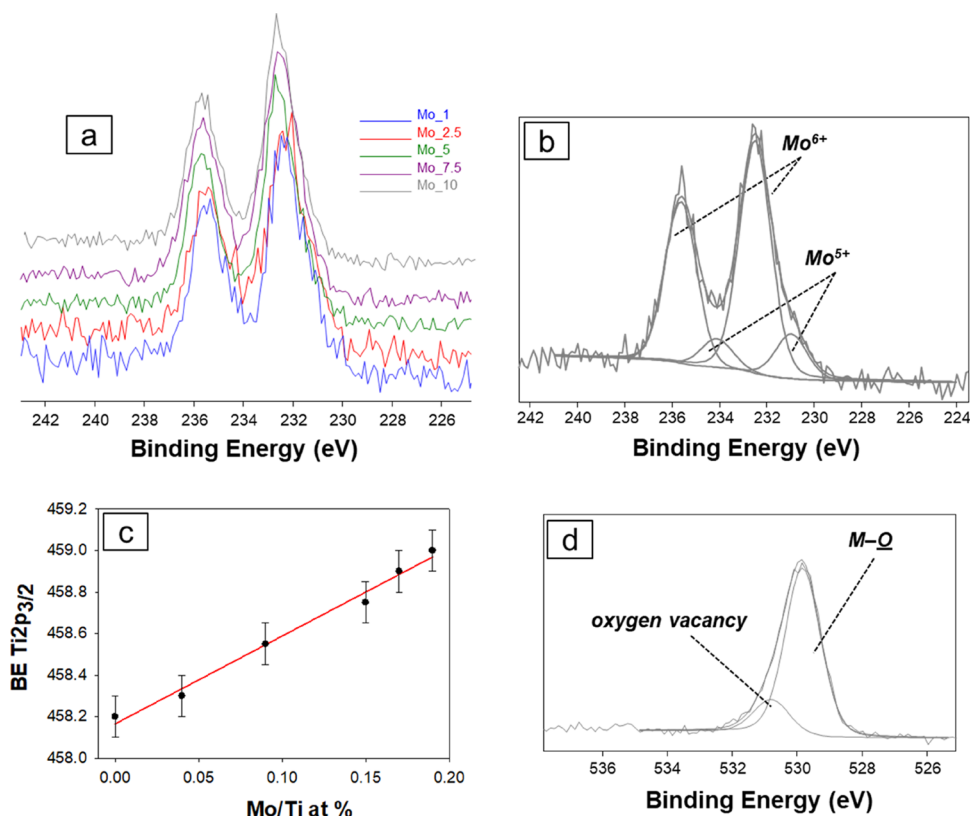
Figure 6. Comparison of the Mo3d XP spectra of the Mo-doped samples (a); Mo3d XP spectrum and related curve-fitting results as obtained with the Mo_2.5 sample (b); Ti2p$_{3/2}$ BE peak position *vs* surface Mo/Ti at. % (c); O1s XP spectrum and the related curve-fitting for the Mo_7.5 sample (d).

values being reported in Table 2) that, in turn, was used to determine the CB position, by considering the E_g values determined by DR UV−vis spectroscopy (*vide infra*).

DR UV−vis spectra (Figure 7a) show a redshift of the onset of absorption with Mo doping, along with a broad absorption band in the d-d transition range. As expected, the TiO$_2$ sample absorbed below 400 nm, whereas the introduction of Mo brought about two effects: a slight redshift of the absorption edge and the appearance of a broad absorption centered at ca. 550 nm, readily assigned to the sub-band transitions related to midband gaps formed by Mo doping.[57]

The redshift of the absorption edge shows that Mo doping is modifying the materials' E_g values that were here calculated by the Tauc's plot method (not shown) for the indirect semiconductor, anatase being the most abundant polymorph (Table 2). The smallest E_g value was obtained with the Mo_7.5 sample, then an E_g increase occurred at a higher Mo content. Figure 7b shows the E_g values along with the position of VB samples, as determined by the XPS analysis and CB values calculated as (VB + E_g). Interestingly, when a template-free sol−gel method was adopted to obtain Mo-doped TiO$_2$ with a similar composition, the effect on the E_g was ca. 10% smaller, especially at higher Mo contents, showing that here the reported reverse micelle sol−gel synthesis may lead to a remarkable decrease in E_g.[33] The figure also shows that the Mo introduction modifies the position of both the VB and the CB and that at a higher Mo content, an increase in E_g is observed. The latter phenomenon can be due to the occurrence of the Moss−Burstein (or Burstein−Moss) effect, *i.e.*, the apparent increase of a semiconductor band gap, due to the fact that at high doping levels, some states close to the CB are being

populated.[58] When the electron carrier concentration exceeds the CB edge density of the states, degenerate doping in semiconductors occurs: here, it shows that the adopted synthesis method allowed such an effective inclusion of Mo in the TiO$_2$ matrix that the Moss−Burstein effect was observed.

Indeed, such an effect, *i.e.*, an (unexpected) increase in the E_g at a higher amount of dopant had been already observed in Mo-doped TiO$_2$ NPs[13] which, at an intermediate Mo content, were active toward the photocatalytic degradation of rhodamine B (a model water pollutant) under simulated solar light, showing that this type of doped TiO$_2$ has indeed appealing photocatalytic properties, in agreement with the literature in the field.[59−61] In perspective, such an effective doping procedure could be applied not only to introduce other types of doping elements within TiO$_2$ matrices but also to synthesize other types of materials, like doped ZnO, which is along with TiO$_2$, the most studied semiconductors with many and diverse applications in photocatalysis and biology as an antibacterial, etc., as acknowledged by the literature.[62−64]

■ CONCLUSIONS

The obtained results allowed inferring a prominent role of the adopted synthesis technique on the samples' physicochemical properties in that reverse micelle sol−gel synthesis allowed the inclusion of a sizeable amount of Mo in the bulk, with a consequent modification of the VB and CB of the final material. The type of synthesis also affected the kind of mixed phases occurring in the final product (anatase, brookite, and rutile, the last one at Mo wt % ≥2.5) as well as the surface
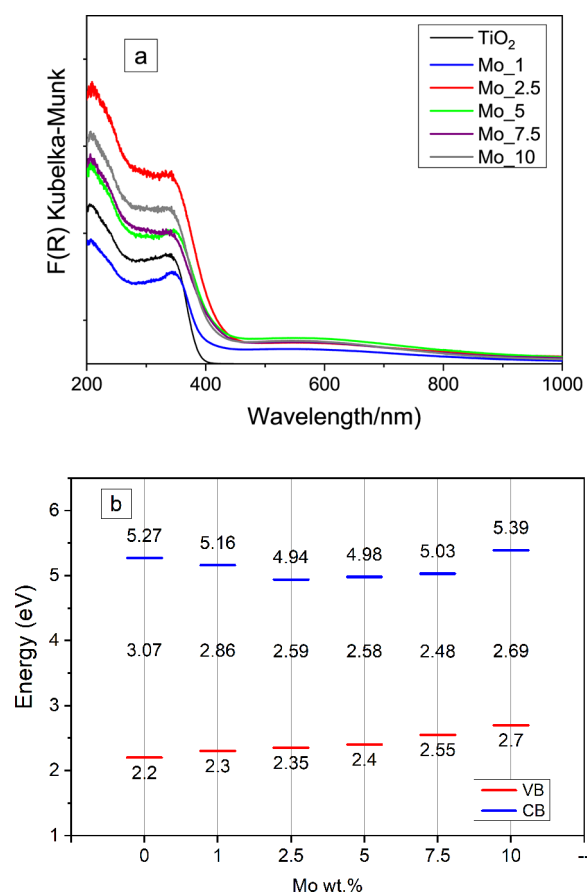
Figure 7. DR UV−vis spectra of the studied samples in the 200−1000 nm range (a); energy of the VB, as determined by XPS and of the CB, as obtained by (VB + E_g).

species in the samples' surface is extremely acidic especially when Mo doping occurs.

The surface species were also studied by the XPS analysis, showing the occurrence of both Mo^{6+} and Mo^{5+} species, the latter forming, along with oxygen vacancies, in order to balance the extra positive charge induced by doping.

The energies of both the VB and CB were determined by means of the joint use of DR UV−vis and XPS, showing the occurrence of the Moss−Burstein effect at the highest Mo content, as a consequence of the extremely effective inclusion of Mo in the NPs due to the type of synthesis. The reverse micelles containing the system likely allowed the ultimate mixing of both Ti and Mo precursors and could be used to include other types of metals, which instead tend to form defects and/or aggregates (e.g., Fe), with a detrimental effect on photocatalytic applications.

■ EXPERIMENTAL SECTION

Synthesis Method. Undoped and Mo-doped TiO_2 NPs were prepared by a sol−gel reverse micelle microemulsion method[65] by using polyoxyethylene (20) oleyl ether, Brij O20 as a surfactant, cyclohexane as an oil phase, titanium(IV) butoxide 97% (Ti-$(BuO)_4$), and ammonium heptamolybdate tetrahydrate (($NH_4)_6Mo_7O_{24}*4H_2O$, Sigma-Aldrich, purum p.a. > = 99.9%) as Ti and Mo precursors, respectively.

The proper precursor amounts were used in order to obtain Mo wt % nominal contents of 0.0, 1.0, 2.5, 5.0, 7.5, and 10. A typical synthesis involves the following steps: the surfactant is

dispersed in cyclohexane by stirring at 50 °C, while the salt precursor is dissolved in Milli-Q water at the same temperature. Afterward, the salt solution is added to the oil/surfactant mixture and stirred for 45 min, with the formation of a water-in-oil (w/o) microemulsion of surfactant nanoreactors. The TiO_2 precursor is then dropwise added to the emulsion. The mixture is stirred for 2 h at the constant temperature of 50.0 °C and finally, the emulsion is broken by the addition of 2-propanol, followed by sonication. The solid is collected by centrifugation and dried at 100 °C for 24 h, followed by calcination in air at 500 °C for 2 h with a temperature ramp of 2.5 °C min^{-1} to remove the surfactant.

Characterization Methods. Powder X-ray diffraction (PXRD) patterns were obtained by using an X'Pert Phillips diffractometer operating at 40 kV and 40 mA with Cu Kα radiation (scanning resolution $2\theta = 0.026°$, time per step: 2 s). The samples' phase composition and structural parameters were determined by the Rietveld analysis as implemented in the MAUD software.[66] Instrumental broadening was characterized by the NIST standard 660a (LaB_6).

The Raman spectra were taken by a Renishaw InVia Reflex micro-Raman spectrometer equipped with a cooled charge-coupled device (CCD) camera; the source was a diode laser ($\lambda_{ex} = 514$ nm); and powders were pressed into self-supporting wafers to ensure the inspection of a flat surface by means of a microscope objective (100X) in a backscattering light collection mode (laser power: 0.5 mW; exposure time: 10 s; 1 accumulation).

The field-emission scanning electron microscopy (FE-SEM) images were taken by a ZEISS Supra 40 FESEM instrument equipped with an energy-dispersive X-ray (EDX) probe; the latter was used for the (semiquantitative) analysis of the sample chemical composition on 5 μm^3 volume spots; and EDX maps were also measured in order to determine the dispersion of Ti, O, and Mo in the NPs.

N_2 adsorption/desorption isotherms at −196 °C were measured on samples previously outgassed at 120 °C for 1 h and then at 150 °C for 2 h (Micromeritics ASAP 2020 Plus instrument). The samples' specific surface area (SSA) was calculated by applying the Brunauer−Emmett−Teller (BET) method; pore total volume was measured at $P/P^0 = 0.99$; and the pore size distribution and cumulative pore volumes were determined by the density functional theory (DFT) method through a N_2/oxide surface kernel for the cylindrical pores.

The diffuse reflectance (DR) UV−visible spectra were recorded by a UV−vis Varian Cary 5000 spectrophotometer equipped with an integration sphere for the DR measurements. The samples' band gap energy (E_g) was then calculated by applying the Tauc's plot method for the indirect semiconductors.

The surface chemical composition and speciation were investigated by X-ray photoelectron spectroscopy (XPS) using a Versa Probe II scanning XPS microprobe spectrometer (Physical Electronics GmbH), equipped with a monochromatized Al Kα source (X-ray spot = 100 μm) at a power of 26.7 W. Both wide scans and high-resolution XP spectra were acquired using a fixed analyzer transmission (FAT) mode with pass energies of 117.40 and 29.35 eV, respectively. An electron gun was used for the charge compensation (1.0 V 20.0 μA). The data processing was performed by using MultiPak software version 9.9.0.8.

The samples' electrophoretic mobility was measured using a Zetasizer Nano ZSP instrument (Malvern Instruments Ltd.,

GB) on mixtures prepared by adding ca. 5 mg of powder to 10 mL of bi-distilled water and then sonicating for 5 min; during the measurements, pH was adjusted by the addition of either HCl or NH$_4$OH aqueous solutions. The samples' ζ potential was obtained from the electrophoretic mobility by applying the Smoluchowski's approximation.

ASSOCIATED CONTENT

Supporting Information

The Supporting Information is available free of charge at https://pubs.acs.org/doi/10.1021/acsomega.0c05552.

Micro-Raman spectra (Figure S1); FE-SEM micrographs (Figure S2); and EDX elemental maps (Figure S3) (PDF)

AUTHOR INFORMATION

Corresponding Author

Barbara Bonelli — *Department of Applied Science and Technology, Politecnico di Torino, Torino I-10129, Italy; INSTM Unit of Torino-Politecnico, Torino I-10129, Italy;* orcid.org/0000-0002-4716-864X; Email: barbara.bonelli@polito.it

Authors

Serena Esposito — *Department of Applied Science and Technology, Politecnico di Torino, Torino I-10129, Italy; INSTM Unit of Torino-Politecnico, Torino I-10129, Italy;* orcid.org/0000-0001-9159-0541

Nicoletta Ditaranto — *Dipartimento di Chimica, Università degli Studi di Bari "Aldo Moro", Bari 70125, Italy*

Gianfranco Dell'Agli — *Dipartimento di Ingegneria Civile e Meccanica, Università degli Studi di Cassino e del Lazio Meridionale, Cassino (FR) I-03043, Italy*

Roberto Nasi — *Department of Applied Science and Technology, Politecnico di Torino, Torino I-10129, Italy*

Paola Rivolo — *Department of Applied Science and Technology, Politecnico di Torino, Torino I-10129, Italy;* orcid.org/0000-0003-0672-5793

Complete contact information is available at: https://pubs.acs.org/10.1021/acsomega.0c05552

Notes

The authors declare no competing financial interest.

REFERENCES

(1) Hoffmann, M. R.; Martin, S. T.; Choi, W.; Bahnemann, D. W. Environmental Applications of Semiconductor Photocatalysis. *Chem. Rev.* **1995**, *95*, 69−96.

(2) Linsebigler, A. L.; Lu, G.; Yates, J. T., Jr. Photocatalysis on TiO2 Surfaces: Principles, Mechanisms, and Selected Results. *Chem. Rev.* **1995**, *95*, 735−758.

(3) Chen, X.; Mao, S. S. Titanium Dioxide Nanomaterials: Synthesis, Properties, Modifications and Applications. *Chem. Rev.* **2007**, *107*, 2891−2959.

(4) Bonelli, B.; Esposito, S.; Freyria, F. S. Mesoporous Titania: Synthesis, Properties and Comparison with Non-Porous Titania. In *Titanium Dioxide*; Janus, M., Ed.; Intech, 2017.

(5) Bonelli, B.; Cozzolino, M.; Tesser, R.; Di Serio, M.; Piumetti, M.; Garrone, E.; Santacesaria, E. Study of the Surface Acidity of TiO2/SiO2 Catalysts by Means of FTIR Measurements of CO and NH3 Adsorption. *J. Catal.* **2007**, *246*, 293.

(6) Kavan, L.; Grätzel, M.; Gilbert, S. E.; Klemenz, C.; Scheel, H. J. Electrochemical and Photoelectrochemical Investigation of Single-Crystal Anatase. *J. Am. Chem. Soc.* **1996**, 6716.

(7) Reyes-Coronado, D.; Rodríguez-Gattorno, G.; Espinosa-Pesqueira, M. E.; Cab, C.; De Coss, R.; Oskam, G. Phase-Pure TiO2 Nanoparticles: Anatase, Brookite and Rutile. *Nanotechnology* **2008**, *19*, 145605.

(8) Asahi, R.; Taga, Y.; Mannstadt, W.; Freeman, A. J. Electronic and Optical Properties of Anatase TiO2. *Phys. Rev. B - Condens. Matter Mater. Phys.* **2000**, *61*, 7459−7465.

(9) Moma, J.; Baloyi, J. Modified Titanium Dioxide for Photo-catalytic Applications. In *Photocatalysts - Applications and Attributes*; IntechOpen, 2018. DOI: 10.5772/intechopen.79374.

(10) Clarizia, L.; Vitiello, G.; Pallotti, D. K.; Silvestri, B.; Nadagouda, M.; Lettieri, S.; Luciani, G.; Andreozzi, R.; Maddalena, P.; Marotta, R. Effect of Surface Properties of Copper-Modified Commercial Titanium Dioxide Photocatalysts on Hydrogen Production through Photoreforming of Alcohols. *Int. J. Hydrogen Energy* **2017**, *42*, 28349−28362.

(11) Piumetti, M.; Freyria, F. S.; Armandi, M.; Geobaldo, F.; Garrone, E.; Bonelli, B. Fe- and V-Doped Mesoporous Titania Prepared by Direct Synthesis: Characterization and Role in the Oxidation of AO7 by H2O2 in the Dark. *Catal. Today* **2014**, *227*, 71.

(12) Freyria, F. S.; Compagnoni, M.; Ditaranto, N.; Rossetti, I.; Piumetti, M.; Ramis, G.; Bonelli, B. Pure and Fe-Doped Mesoporous Titania Catalyse the Oxidation of Acid Orange 7 by H2O2 under Different Illumination Conditions: Fe Doping Improves Photo-catalytic Activity under Simulated Solar Light. *Catalysts* **2017**, *7*, 213.

(13) Nasi, R.; Esposito, S.; Freyria, F. S.; Armandi, M.; Gadhi, T. A.; Hernandez, S.; Rivolo, P.; Ditaranto, N.; Bonelli, B. Application of Reverse Micelle Sol − Gel Synthesis for Bulk Doping and Heteroatoms Surface Enrichment In Mo-Doped TiO2 Nanoparticles. *Materials* **2019**, *12*, 937.

(14) Fang, J.; Wang, F.; Qian, K.; Bao, H.; Jiang, Z.; Huang, W. Bifunctional N-Doped Mesoporous TiO 2 Photocatalysts. *J. Phys. Chem. C* **2008**, *112*, 18150−18156.

(15) Hossain, M. A.; Elias, M.; Sarker, D. R.; Diba, Z. R.; Mithun, J. M.; Azad, M. A. K.; Siddiquey, I. A.; Rahman, M. M.; Uddin, J.; Uddin, M. N. Synthesis of Fe- or Ag-Doped TiO2−MWCNT Nanocomposite Thin Films and Their Visible-Light-Induced Catalysis of Dye Degradation and Antibacterial Activity. *Res. Chem. Intermed.* **2018**, *44*, 2667−2683.

(16) Guayaquil-Sosa, J. F.; Serrano-Rosales, B.; Valadés-Pelayo, P. J.; de Lasa, H. Photocatalytic Hydrogen Production Using Mesoporous TiO2 Doped with Pt. *Appl. Catal. B Environ.* **2017**, *211*, 337−348.

(17) Petrie, B.; Barden, R.; Kasprzyk-hordern, B. A Review on Emerging Contaminants in Wastewaters and the Environment : Current Knowledge , Understudied Areas and Recommendations for Future Monitoring. *Water Res.* **2015**, *72*, 3−27.

(18) Freyria, F. S.; Blangetti, N.; Esposito, S.; Nasi, R.; Armandi, M.; Annelio, V.; Bonelli, B. Effects of the Brookite Phase on the Properties of Different Nanostructured TiO2 Phases Photocatalytically Active Towards the Degradation of N-Phenylurea. *ChemistryOpen* **2020**, 903−912.

(19) Navrotsky, A. Energetics of Nanoparticle Oxides: Interplay between Surface Energy and Polymorphism. *Geochem. Trans.* **2003**, 34−37.

(20) Zhang, J.; Zhou, P.; Liu, J.; Yu, J. New Understanding of the Difference of Photocatalytic Activity among Anatase, Rutile and Brookite TiO 2. *Phys. Chem. Chem. Phys.* **2014**, *16*, 20382−20386.

(21) Vequizo, J. J. M.; Matsunaga, H.; Ishiku, T.; Kamimura, S.; Ohno, T.; Yamakata, A. Trapping-Induced Enhancement of Photo-

catalytic Activity on Brookite TiO2 Powders: Comparison with Anatase and Rutile TiO2 Powders. *ACS Catal.* **2017**, *7*, 2644−2651.

(22) Monai, M.; Montini, T.; Fornasiero, P. Brookite: Nothing New under the Sun? *Catalysts* **2017**, *7*, 304.

(23) Bonelli, B.; Onida, B.; Chen, J. D.; Galarneau, A.; Di Renzo, F.; Fajula, F.; Garrone, E. Spectroscopic Characterisation of the Strength and Stability of the Acidic Sites of Al-Rich Microporous Micelle-Templated Silicates. *Microporous Mesoporous Mater.* **2004**, *67*, 95.

(24) Ma, Y.; Wang, X.; Jia, Y.; Chen, X.; Han, H.; Li, C. Titanium Dioxide-Based Nanomaterials for Photocatalytic Fuel Generations. *Chem. Rev.* **2014**, *114*, 9987−10043.

(25) Houng, B.; Liu, C. C.; Hung, M. T. Structural, Electrical and Optical Properties of Molybdenum-Doped TiO 2 Thin Films. *Ceram. Int.* **2013**, *39*, 3669−3676.

(26) Khan, A. Q.; Yuan, S.; Niu, S.; Zheng, L.; Li, W.; Zeng, H. Synthesis of Molybdenum Oxide-Titanium Dioxide Nanocomposites with Ultrashort Laser Ablation in Water. *Opt. Express* **2017**, *25*, A539.

(27) Shahmoradi, B.; Ibrahim, I. A.; Sakamoto, N.; Ananda, S.; Guru Row, T. N.; Soga, K.; Byrappa, K.; Parsons, S.; Shimizu, Y. In Situ Surface Modification of Molybdenum-Doped Organic-Inorganic Hybrid TiO2 Nanoparticles under Hydrothermal Conditions and Treatment of Pharmaceutical Effluent. *Environ. Technol.* **2010**, *31*, 1213−1220.

(28) Avilés-García, O.; Espino-Valencia, J.; Romero-Romero, R.; Rico-Cerda, J.; Arroyo-Albiter, M.; Solís-Casados, D. A.; Natividad-Rangel, R. Enhanced Photocatalytic Activity of Titania by Co-Doping with Mo and W. *Catalysts* **2018**, *8*, 631.

(29) Wang, S.; Bai, L. N.; Sun, H. M.; Jiang, Q.; Lian, J. S. Structure and Photocatalytic Property of Mo-Doped TiO2 Nanoparticles. *Powder Technol.* **2013**, *244*, 9−15.

(30) Sarkar, S.; Choudhury, P.; Dinda, S.; Das, P. K. Tailor-Made Self-Assemblies from Functionalized Amphiphiles: Diversity and Applications. *Langmuir* **2018**, *34*, 10449−10468.

(31) Uskoković, V.; Drofenik, M. Reverse Micelles: Inert Nano-Reactors or Physico-Chemically Active Guides of the Capped Reactions. *Adv. Colloid Interface Sci.* **2007**, *133*, 23−34.

(32) Khan, M.; Xu, J.; Cao, W.; Liu, Z.-K. Mo-Doped TiO2 with Enhanced Visible Light Photocatalytic Activity: A Combined Experimental and Theoretical Study. *J. Nanosci. Nanotechnol.* **2014**, *14*, 6865−6871.

(33) Bhattacharyya, K.; Majeed, J.; Dey, K. K.; Ayyub, P.; Tyagi, A. K.; Bharadwaj, S. R. Effect of Mo-Incorporation in the TiO2 Lattice: A Mechanistic Basis for Photocatalytic Dye Degradation. *J. Phys. Chem. C* **2014**, *118*, 15946−15962.

(34) Majeed, J.; Nayak, C.; Jha, S. N.; Bhattacharyya, K.; Bhattacharyya, D.; Tripathi, A. K. Correlation of Mo Dopant and Photocatalytic Properties for Mo Incorporated TiO2: An EXAFS and Photocatalytic Study. *RSC Adv.* **2015**, *5*, 90932−90940.

(35) Feng, Y. J.; Wang, C.; Cheng, W. R.; Huang, J. H.; Zhao, T. X.; Liu, Q. H.; Xie, Z.; Pan, Z. Y.; Wei, S. Q. Local Structure of Mo-Doped TiO2 Photocatalysts Investigated by X-Ray Absorption Fine Structure. *J. Phys. Conf. Ser.* **2013**, *430*, 012090.

(36) Hanaor, D. A. H.; Sorrell, C. C. Review of the Anatase to Rutile Phase Transformation. *J. Mater. Sci.* **2011**, *46*, 855−874.

(37) Mutuma, B. K.; Shao, G. N.; Duck, W.; Taik, H.; Kim, H. T. Sol − Gel Synthesis of Mesoporous Anatase − Brookite and Anatase − Brookite − Rutile TiO2 Nanoparticles and Their Photocatalytic Properties. *J. Colloid Interface Sci.* **2015**, *442*, 1−7.

(38) Kibasomba, P. M.; Dhlamini, S.; Maaza, M.; Liu, C. P.; Rashad, M. M.; Rayan, D. A.; Mwakikunga, B. W. Strain and Grain Size of TiO2 Nanoparticles from TEM, Raman Spectroscopy and XRD: The Revisiting of the Williamson-Hall Plot Method. *Results Phys.* **2018**, *9*, 628−635.

(39) Hearne, G. R.; Zhao, J.; Dawe, A. M.; Pischedda, V.; Maaza, M.; Nieuwoudt, M. K.; Kibasomba, P.; Nemraoui, O.; Comins, J. D.; Witcomb, M. J. Effect of Grain Size on Structural Transitions in Anatase TiO2: A Raman Spectroscopy Study at High Pressure. *Phys. Rev. B - Condens. Matter Mater. Phys.* **2004**, *70*, 1−10.

(40) Dakka, A.; Lafait, J.; Sella, C.; Berthier, S.; Abd-Lefdil, M.; Martin, J. C.; Maaza, M. Optical Properties of Ag−TiO2 Nanocermet Films Prepared by Cosputtering and Multilayer Deposition Techniques. *Appl. Opt.* **2000**, *39*, 2745−2753.

(41) Kubacka, A.; Colón, G.; Fernández-García, M. Cationic (V, Mo, Nb, W) Doping of TiO2-Anatase: A Real Alternative for Visible Light-Driven Photocatalysts. *Catal. Today* **2009**, *143*, 286−292.

(42) Ghosh, S. Comparative Studies on Brij Reverse Micelles Prepared in Benzene/Surfactant/Ethylammonium Nitrate Systems: Effect of Head Group Size and Polarity of the Hydrocarbon Chain. *J. Colloid Interface Sci.* **2011**, *360*, 672−680.

(43) Hu, Y.; Tsai, H. L.; Huang, C. L. Effect of Brookite Phase on the Anatase-Rutile Transition in Titania Nanoparticles. *J. Eur. Ceram. Soc.* **2003**, *23*, 691−696.

(44) Ŝtengl, V.; Bakardjieva, S. Molybdenum-Doped Anatase and Its Extraordinary Photocatalytic Activity in the Degradation of Orange II in the UV and Vis Regions. *J. Phys. Chem. C* **2010**, *114*, 19308−19317.

(45) Gomathi Devi, L.; Narasimha Murhty, B.; Girish Kumar, S. Photo Catalytic Degradation of Imidachloprid under Solar Light Using Metal Ion Doped TiO2 Nano Particles: Influence of Oxidation State and Electronic Configuration of Dopants. *Catal. Letters* **2009**, *130*, 496−503.

(46) Thi, T. V.; Rai, A. K.; Gim, J.; Kim, S.; Kim, J. Effect of Mo6+ Doping on Electrochemical Performance of Anatase TiO2 as a High Performance Anode Material for Secondary Lithium-Ion Batteries. *J. Alloys Compd.* **2014**, *598*, 16−22.

(47) Wang, X. H.; Li, J. G.; Kamiyama, H.; Ishigaki, T. Fe-Doped TiO2 Nanopowders by Oxidative Pyrolysis of Organometallic Precursors in Induction Thermal Plasma: Synthesis and Structural Characterization. *Thin Solid Films* **2006**, *506-507*, 278−282.

(48) Batzill, M.; Morales, E. H.; Diebold, U. Influence of Nitrogen Doping on the Defect Formation and Surface Properties of TiO2 Rutile and Anatase. *Phys. Rev. Lett.* **2006**, *96*, 026103.

(49) Al-Hetlani, E.; Amin, M. O.; Madkour, M. Detachable Photocatalysts of Anatase TiO2 Nanoparticles: Annulling Surface Charge for Immediate Photocatalyst Separation. *Appl. Surf. Sci.* **2017**, *411*, 355−362.

(50) He, H.; Cheng, Y.; Yang, C.; Zeng, G.; Zhu, C.; Yan, Z. Influences of Anion Concentration and Valence on Dispersion and Aggregation of Titanium Dioxide Nanoparticles in Aqueous Solutions. *J. Environ. Sci.* **2017**, *54*, 135−141.

(51) Holmberg, J. P.; Ahlberg, E.; Bergenholtz, J.; Hassellöv, M.; Abbas, Z. Surface Charge and Interfacial Potential of Titanium Dioxide Nanoparticles: Experimental and Theoretical Investigations. *J. Colloid Interface Sci.* **2013**, *407*, 168−176.

(52) Suttiponparnit, K.; Jiang, J.; Sahu, M.; Suvachittanont, S.; Charinpanitkul, T.; Biswas, P. Role of Surface Area, Primary Particle Size, and Crystal Phase on Titanium Dioxide Nanoparticle Dispersion Properties. *Nanoscale Res. Lett.* **2010**, *6*, 27.

(53) Honary, S.; Zahir, F. Effect of Zeta Potential on the Properties of Nano-Drug Delivery Systems - A Review (Part 2). *Trop. J. Pharm. Res.* **2013**, *12*, 265−273.

(54) Wagner, D.; Naumkin, A. V.; Kraut-Vass, A.; Allison, J. W.; Powell, C. J.; Rumble, J. R., Jr. *NIST Standard Reference Database 20, Version 3.4 (web version)*. 2003, https://srdata.nist.gov/xps/.

(55) Kim, K.; Park, S. Y.; Lim, K. H.; Shin, C.; Myoung, J. M.; Kim, Y. S. Low Temperature and Solution-Processed Na-Doped Zinc Oxide Transparent Thin Film Transistors with Reliable Electrical Performance Using Methanol Developing and Surface Engineering. *J. Mater. Chem.* **2012**, *22*, 23120−23128.

(56) Bong, H.; Lee, W. H.; Lee, D. Y.; Kim, B. J.; Cho, J. H.; Cho, K. High-Mobility Low-Temperature ZnO Transistors with Low-Voltage Operation. *Appl. Phys. Lett.* **2010**, *96*, 192115.

(57) Gomathi Devi, L.; Narasimha Murthy, B. Characterization of Mo Doped TiO2 and Its Enhanced Photo Catalytic Activity Under Visible Light. *Catal. Lett.* **2008**, *125*, 320−330.

(58) Munir, S.; Shah, S. M.; Hussain, H.; Khan, A. R. Effect of Carrier Concentration on the Optical Band Gap of TiO2 Nanoparticles. *Mater. Des.* **2016**, *92*, 64−72.

(59) Gao, B.; Sun, M.; Ding, W.; Ding, Z.; Liu, W. Decoration of γ-Graphyne on TiO2 Nanotube Arrays: Improved Photoelectrochemical and Photoelectrocatalytic Properties. *Appl. Catal., B* **2021**, *281*, 119492.

(60) Yao, Y.; Sun, M.; Yuan, X.; Zhu, Y.; Lin, X.; Anandan, S. One-Step Hydrothermal Synthesis of N/Ti3+ Co-Doping Multiphasic TiO2/BiOBr Heterojunctions towards Enhanced Sonocatalytic Performance. *Ultrason. Sonochem.* **2018**, *49*, 69−78.

(61) Lin, X.; Sun, M.; Gao, B.; Ding, W.; Zhang, Z.; Anandan, S.; Umar, A. Hydrothermally Regulating Phase Composition of TiO2 Nanocrystals toward High Photocatalytic Activity. *J. Alloys Compd.* **2021**, *850*, 156653.

(62) Karthik, S.; Siva, P.; Balu, K. S.; Suriyaprabha, R.; Rajendran, V.; Maaza, M. Acalypha Indica−Mediated Green Synthesis of ZnO Nanostructures under Differential Thermal Treatment: Effect on Textile Coating, Hydrophobicity, UV Resistance, and Antibacterial Activity. *Adv. Powder Technol.* **2017**, *28*, 3184−3194.

(63) Khalil, A. T.; Ovais, M.; Ullah, I.; Ali, M.; Shinwari, Z. K.; Khamlich, S.; Maaza, M. Sageretia Thea (Osbeck.) Mediated Synthesis of Zinc Oxide Nanoparticles and Its Biological Applications. *Nanomedicine* **2017**, *12*, 1767−1789.

(64) Kaviyarasu, K.; Magdalane, C. M.; Manikandan, E.; Jayachandran, M.; Ladchumananandasivam, R.; Neelamani, S.; Maaza, M. Well-Aligned Graphene Oxide Nanosheets Decorated with Zinc Oxide Nanocrystals for High Performance Photocatalytic Application. *Int. J. Nanosci.* **2015**, *14*, 1550007.

(65) Eastoe, J.; Hollamby, M. J.; Hudson, L. Recent Advances in Nanoparticle Synthesis with Reversed Micelles. *Adv. Colloid Interface Sci.* **2006**, *128-130*, 5−15.

(66) Lutterotti, L.; Bortolotti, M.; Ischia, G.; Lonardelli, I.; Wenk, H. R. Rietveld Texture Analysis from Diffraction Images. *Z. Krist. Suppl.* **2007**, *2007*, 125−130.